The relationship between birth timing, circuit wiring, and physiological response properties of cerebellar granule cells

S. Andrew Shuster[a,b,c,1], Mark J. Wagner[a,b,1], Nathan Pan-Doh[a,b], Jing Ren[a,b,d], Sophie M. Grutzner[a,b], Kevin T. Beier[a,b,e], Tony Hyun Kim[a,b,f], Mark J. Schnitzer[a,b,f], and Liqun Luo[a,b,2]

[a]HHMI, Stanford University, Stanford, CA 94305; [b]Department of Biology, Stanford University, Stanford, CA 94305; [c]Neurosciences Graduate Program, Stanford University, Stanford, CA 94305; [d]Medical Research Council Laboratory of Molecular Biology, Cambridge University, Cambridge CB2 0QH, United Kingdom; [e]Department of Physiology and Biophysics, University of California, Irvine, CA 92697; and [f]Department of Applied Physics, Stanford University, Stanford, CA 94305

Contributed by Liqun Luo, April 29, 2021 (sent for review January 28, 2021; reviewed by Michael Häusser and Roy Sillitoe)

Cerebellar granule cells (GrCs) are usually regarded as a uniform cell type that collectively expands the coding space of the cerebellum by integrating diverse combinations of mossy fiber inputs. Accordingly, stable molecularly or physiologically defined GrC subtypes within a single cerebellar region have not been reported. The only known cellular property that distinguishes otherwise homogeneous GrCs is the correspondence between GrC birth timing and the depth of the molecular layer to which their axons project. To determine the role birth timing plays in GrC wiring and function, we developed genetic strategies to access early- and late-born GrCs. We initiated retrograde monosynaptic rabies virus tracing from control (birth timing unrestricted), early-born, and late-born GrCs, revealing the different patterns of mossy fiber input to GrCs in vermis lobule 6 and simplex, as well as to early- and late-born GrCs of vermis lobule 6: sensory and motor nuclei provide more input to early-born GrCs, while basal pontine and cerebellar nuclei provide more input to late-born GrCs. In vivo multidepth two-photon Ca^{2+} imaging of axons of early- and late-born GrCs revealed representations of diverse task variables and stimuli by both populations, with modest differences in the proportions encoding movement, reward anticipation, and reward consumption. Our results suggest neither organized parallel processing nor completely random organization of mossy fiber→GrC circuitry but instead a moderate influence of birth timing on GrC wiring and encoding. Our imaging data also provide evidence that GrCs can represent generalized responses to aversive stimuli, in addition to recently described reward representations.

cerebellum | granule cells | birth timing | rabies tracing | two-photon Ca^{2+} imaging

Cerebellar granule cells (GrCs) comprise the majority of neurons in the mammalian brain (1, 2). Each GrC receives only four excitatory inputs from mossy fibers, which originate in a variety of brainstem nuclei and the spinal cord, and the vast number of GrCs permits diverse combinations of mossy fiber inputs. Classical theories of cerebellar function have therefore proposed that GrCs integrate diverse, multimodal mossy fiber inputs and thus collectively expand coding space in the cerebellum (3–5). Until recently, studies have focused on the role of GrCs in implementing sparse coding of sensorimotor variables and stimuli (6–9). However, recent physiological studies of GrCs in awake, behaving animals highlight GrC encoding of cognitive signals in addition to sensorimotor signals (10–13). GrCs have also been recently shown to encode denser representations than expected by classical theory (10–12, 14–18), including a lack of dimensionality expansion under certain conditions (18).

Despite the vast number of GrCs, stable molecularly or physiologically defined GrC subtypes within a single cerebellar region or lobule have not been described (19–22), although variation in gene expression across different regions has been reported (22, 23). The only known axis along which spatially intermingled GrCs can be distinguished from each other is the depth of the molecular layer to which their parallel fiber axons (PFs) project, which is dictated by GrC lineage and birth timing (24, 25). Birth timing predicts the wiring and functional properties of diverse neuron types in many neural systems (26), including the neocortex (27, 28), other forebrain regions (29, 30), olfactory bulb (31–33), and ventral spinal cord (34, 35). Furthermore, classic studies utilizing γ-irradiation at different times during rat postnatal development to ablate different cerebellar GrC and interneuron populations suggested that GrCs born at different times could contribute differentially to motor vs. action coordination (36). These observations also led to an as-of-yet untested hypothesis that mossy fibers arriving at different times during development could connect with different GrC populations. Could GrC birth timing be an organizing principle for information processing in the cerebellum?

Recent evidence and modeling point to the possibility of spatial clusters of coactivated PFs (15, 37), suggesting that GrCs born around the same time may disproportionally receive coactive mossy fiber inputs. However, another study using different methods and stimuli did not find differences in the physiological responses of early- and late-born GrCs to various sensorimotor stimuli (38). Here, we address the role of birth timing in GrC wiring and function.

Significance

Cerebellar granule cells (GrCs) comprise the majority of all neurons in the mammalian brain and are usually regarded as a uniform cell type. However, the birth timing of individual GrCs dictates where their axons project. Using viral-genetic techniques, we find that early- and late-born GrCs receive different proportions of inputs from the same set of input regions. In vivo multidepth two-photon Ca^{2+} imaging of axons of early- and late-born GrCs reveals that both populations represent diverse task variables and stimuli, with small differences in the proportions of axons in encoding of a subset of movement and reward parameters. These results indicate that birth timing makes a modest contribution to the input selection and physiological response properties of GrCs.

Author contributions: S.A.S., M.J.W., and L.L. designed research; S.A.S., M.J.W., N.P.-D., and S.M.G. performed research; J.R., K.T.B., T.H.K., and M.J.S. contributed new reagents/analytic tools; S.A.S. and M.J.W. analyzed data; S.A.S., M.J.W., and L.L. wrote the paper; and L.L. supervised research.

Reviewers: M.H., University College London; and R.S., Baylor College of Medicine.

The authors declare no competing interest.

[1]S.A.S. and M.J.W. contributed equally to this work.

[2]To whom correspondence may be addressed. Email: lluo@stanford.edu.

This article contains supporting information online at https://www.pnas.org/lookup/suppl/doi:10.1073/pnas.2101826118/-/DCSupplemental.

Published June 4, 2021.

We developed strategies to gain genetic access to early- and late-born GrCs, as well as control GrCs not restricted by birth timing. We report the first monosynaptic input tracing to GrCs, finding differential mossy fiber inputs to GrCs in vermis lobule 6 and simplex, as well as different patterns of input to early- and late-born GrCs in vermis lobule 6. Finally, we performed in vivo multidepth two-photon Ca^{2+} imaging of PFs of early- and late-born GrCs during an operant task and presentation of a panel of sensory, appetitive, and aversive stimuli. We found modest differences in the proportions of early- and late-born GrCs encoding of a subset of movement and reward parameters. Together, these results reveal a contribution of GrC birth timing to their input wiring and diverse encoding properties.

Results

Genetic Strategies for Accessing Birth-Timing–Defined GrCs. Cerebellar cortical circuit assembly occurs primarily during the first 3 postnatal weeks in the mouse, reaching full maturity shortly thereafter (39). At birth, GrC progenitors occupy the most superficial external granular layer (EGL), where they proliferate. Mossy fibers are morphologically recognizable after postnatal day 5 (P5), shortly after GrC progenitors have begun to exit mitosis (40). Newborn GrCs extend their axons as PFs into the developing molecular layer between the EGL and Purkinje cell bodies, while their somata descend past the Purkinje cell layer (PCL) into the internal granular layer (IGL), giving rise to the granule cell layer in adults

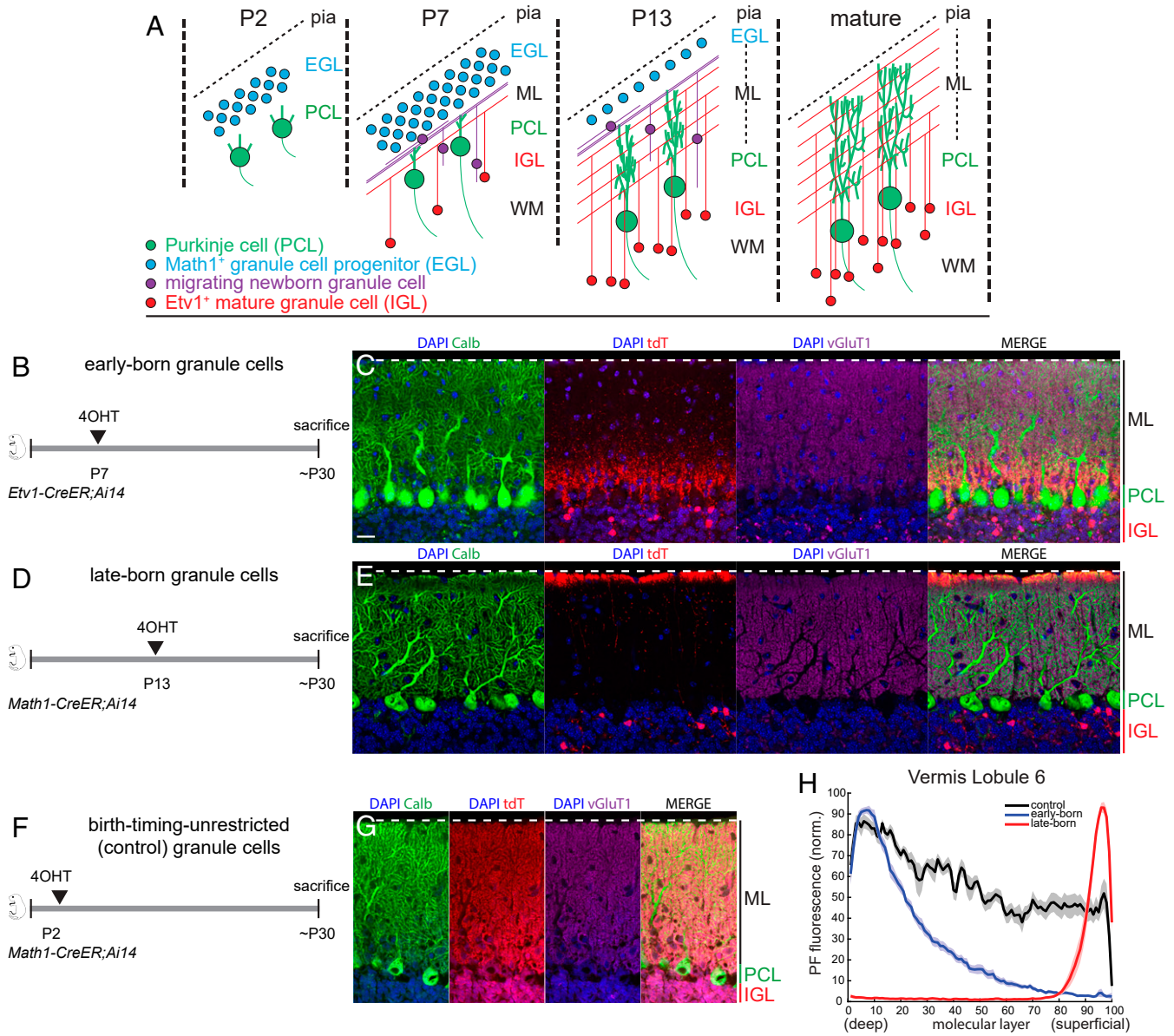

Fig. 1. Genetic strategies for accessing birth-timing–defined cerebellar GrCs. (*A*) Schematic summary of postnatal GrC development. Math1 is expressed in GrC progenitors but not postmitotic GrCs, and Etv1 in postmitotic GrCs but not GrC progenitors. EGL, external granular layer; pia, pia mater; ML, molecular layer; PCL, Purkinje cell layer; IGL, internal granule cell layer; WM, white matter. (*B–G*) Genetic strategies and corresponding images showing PF innervation of the cerebellar molecular layer for access to early-born (*B* and *C*), late-born (*D* and *E*), and birth-timing–unrestricted control (*F* and *G*) GrCs, which project axons (tdT^+) to deep, superficial, and depth-unrestricted portions, respectively, of the molecular layer. Images were taken from vermis lobule 6. Blue, DAPI; green, calbindin, a marker of Purkinje cells; red, tdTomato from the Cre reporter *Ai14*; purple, vGluT1, a marker of PF synapses. Dotted white lines indicate pia surface. (Scale bar, 20 μm.) (*H*) Quantification of PF-derived fluorescence across the depths of the molecular layer in vermis lobule 6. $n = 12$ sections from two mice each.

(41). Later-born GrCs stack their PFs superficially to those of earlier-born GrCs (25). As GrC neurogenesis proceeds, the EGL is gradually replaced by the molecular layer until P21, when GrC neurogenesis is complete (Fig. 1*A*).

To gain access to early- and late-born GrCs, we developed genetic strategies for accessing birth-timing-defined GrCs. We scoured the Allen Brain Atlas transgenic characterization database for CreER lines with expression specific to GrC progenitors and mature GrCs, but not mossy fiber origin sites in the brainstem (42). We identified two lines designed to mimic the expression pattern of the transcription factors *Math1* (43), which is expressed selectively in GrC progenitors in the postnatal cerebellum (44), and *Etv1* (45), which is expressed selectively in postmitotic cerebellar GrCs (*SI Appendix*, Fig. S1). To test our genetic strategies, we crossed *Etv1-CreER* and *Math1-CreER* mice to tdTomato Cre reporter (*Ai14*) mice (46). We injected 4-hydroxytamoxifen (4OHT), the active metabolite of tamoxifen that drives CreER nuclear translocation, into *Etv1-CreER;Ai14* mice at P7 and *Math1-CreER;Ai14* mice at P13 to label early- and late-born GrCs, respectively. As predicted from previous studies (24, 25), these strategies resulted in PF fluorescence selectively in the deep and superficial portions of the molecular layer, respectively (Fig. 1 *B–E*), confirming selective genetic access to early- and late-born GrCs. Furthermore, injecting 4OHT into *Math1-CreER;Ai14* mice at P2 resulted in labeling of GrCs with PFs projecting to all depths of the molecular layer; we used these birth-timing–unrestricted GrCs as a control for comparison with birth-timing–dependent results (Fig. 1 *F* and *G*). Quantitative analysis of PF labeling showed that early- and late-born labeling strategies consistently allowed genetic access to specific and mutually exclusive populations of GrCs, but that the early-born strategy had a longer "tail" and thus more overlap with cells accessed via the control strategy (Fig. 1*H*).

Differential Mossy Fiber Inputs to GrCs in Vermis Lobule 6 and Simplex. To our knowledge, mossy fiber inputs to GrCs from different precerebellar nuclei have not been quantitatively compared, largely due to longstanding technical limitations in performing input tracing from densely packed GrCs. Thus, prior to comparing inputs to early- and late-born GrCs, we first profiled presynaptic mossy fiber inputs to birth-timing–unbiased GrC populations. We applied monosynaptic retrograde rabies virus (RV) tracing (47, 48) of mossy fiber input to GrCs of vermis lobule 6 and simplex. We crossed *Math1-CreER* mice to $R26^{CAG\text{-}LSL\text{-}HTB}$ ($R26^{HTB}$ hereafter) mice (49), which express rabies G protein (B19SAD-RG) and the EnvA receptor TVA in a Cre-dependent manner. We injected *Math1-CreER;*$R26^{HTB}$ mice with 4OHT at P2 and then injected G-deleted, GFP-expressing, EnvA-pseudotyped RV (RVdG-GFP-EnvA) into vermis lobule 6 or simplex (bilateral) at P28 to 33 (Fig. 2*A*). We collected brains 5 d later and quantified GFP-labeled cells (Fig. 2*B*). This analysis revealed inputs from cells in many regions known to originate mossy fibers (50, 51), including the pons, various sensory and motor brainstem nuclei, and the cerebellar nuclei (Fig. 2 *C–M*). In the absence of Cre, there were no retrogradely labeled cells in the brainstem (n = 8 mice); by contrast, the brainstems of experimental animals had thousands of input cells labeled (vermis: 2,285 ± 262 cells; simplex: 2,746 ± 371 cells), validating the specificity of our transgenic-viral tracing methods (*SI Appendix*, Fig. S2*A*).

We grouped inputs into four supercategories: pontine, motor, sensory, and cerebellar nuclei (CN). Pontine input comprises input from the basal pons (BPN) and reticulotegmental nucleus of the pons (RtTg), both of which relay cortical information. Motor nuclei include the prepositus/hypoglossal nuclei (Pre/12N) and the gigantocellular (GRt), intermediate (IRt), parvicellular (PRt), lateral (LRt), and medullary (MRt) nuclei of the brainstem reticular system. Sensory nuclei include the interfascicular (IF5), primary sensory (Pr5), and spinal (Sp5) trigeminal nuclei, the medial (MeVe) and lateral (LaVe) vestibular nuclei, and the external cuneate nucleus (ExC). Among inputs to both vermis lobule 6 and simplex, very few spinal cord and inferior olive (IO) cells were labeled (≪1%), and so were not included in subsequent quantifications.

At the supercategory level, quantitative analysis revealed that vermis lobule 6 received proportionally more pontine input than did simplex, while simplex received proportionally more input in aggregate from sensory brainstem nuclei than did lobule 6 (Fig. 2*I*). Quantitative analysis of individual nuclei revealed differential contributions to lobule 6 and simplex (Fig. 2 *J–M*). For example, within the motor nuclei, lobule 6 received much more input from Pre/12N than did simplex, while simplex received more input from IRt and PRt than did lobule 6 (Fig. 2*L*). Among inputs from sensory nuclei, simplex received more input from trigeminal nuclei (IF5, Pr5, and Sp5) than did lobule 6, while lobule 6 received more input from MeVe than did simplex (Fig. 2*M*). Finally, lobule 6 received a higher proportion of total input from both pontine nuclei (Fig. 2*K*). These results suggest that monosynaptic retrograde rabies virus tracing is sensitive enough to reveal quantitative differences in mossy fiber distributions.

Differential Mossy Fiber Inputs to Early- and Late-Born Lobule 6 GrCs. We next performed monosynaptic retrograde RV tracing to reveal the distributions of mossy fiber input to early- and late-born GrCs. We crossed *Math1-CreER* and *Etv1-CreER* mice to $R26^{HTB}$ mice and injected *Etv1-CreER;*$R26^{HTB}$ and *Math1-CreER;*$R26^{HTB}$ mice with 4OHT at P7 and P13, respectively, to gain access to early- and late-born GrCs, followed by injecting vermis lobule 6 with RVdG-GFP-EnvA. We collected brains 5 d later and analyzed input distributions (Fig. 3*A*). We detected fewer input cells from early- and late-born samples than control samples (early born: 476 ± 54 cells; late born: 440 ± 56 cells; *SI Appendix*, Fig. S3*D*), in accordance with the proportion of GrCs genetically accessed by each strategy (Fig. 1 *C*, *E*, and *G*).

Quantification revealed that late-born GrCs receive more pontine and CN input than early-born GrCs, and less input from motor and sensory nuclei (Fig. 3*B*). Early-born GrCs received similar absolute and within-supercategory proportions of input from all input sources as did control GrCs, possibly due to the early-born population spanning a wider range of birth times than the late-born population (Figs. 1*H* and 3 *B–E* and *SI Appendix*, Fig. S3). The increased pontine input received by late-born GrCs was due to an increase in BPN inputs (Fig. 3*C*). Late-born GrCs also received fewer Pre/12N, LRt, IF5, and ExC inputs than early-born GrCs (Fig. 3 *D* and *E*). Overall, late-born GrCs received more of their within-pontine input from BPN than RtTg (*SI Appendix*, Fig. S3*A*) and less of their within-motor nuclei input from GRt and LRt than early-born GrCs (*SI Appendix*, Fig. S3*B*). These data suggest that late-born GrCs could represent a special population that receives a modified distribution of mossy fiber input or could reflect the greater specificity of our genetic access to late-born compared to early-born GrCs (Fig. 1*H*).

Taken together, these tracing results indicate that all precerebellar nuclei examined provide inputs to both early- and late-born GrCs, but with quantitative differences: sensory and motor nuclei provide more input to early-born GrCs, while basal pontine and cerebellar nuclei provide more to late-born GrCs.

Both Early- and Late-Born Granule Cells Encode Diverse Signals. To address whether GrCs born at different times differ in their response properties toward diverse stimuli, we designed a preparation allowing near-simultaneous two-photon imaging of PF Ca^{2+} activity at two depths while mice performed an operant task (Fig. 4 *A–C*), followed by presentation of a panel of appetitive, aversive, and neutral sensory stimuli (Fig. 4*D* and *Materials and Methods*). To do so, we crossed *Etv1-CreER* mice to *Ai148* mice, which express high levels of GCaMP6f via tTA2/*TRE*-mediated transcriptional activation in a Cre-dependent manner (52). We injected *Etv1-CreER;Ai148*

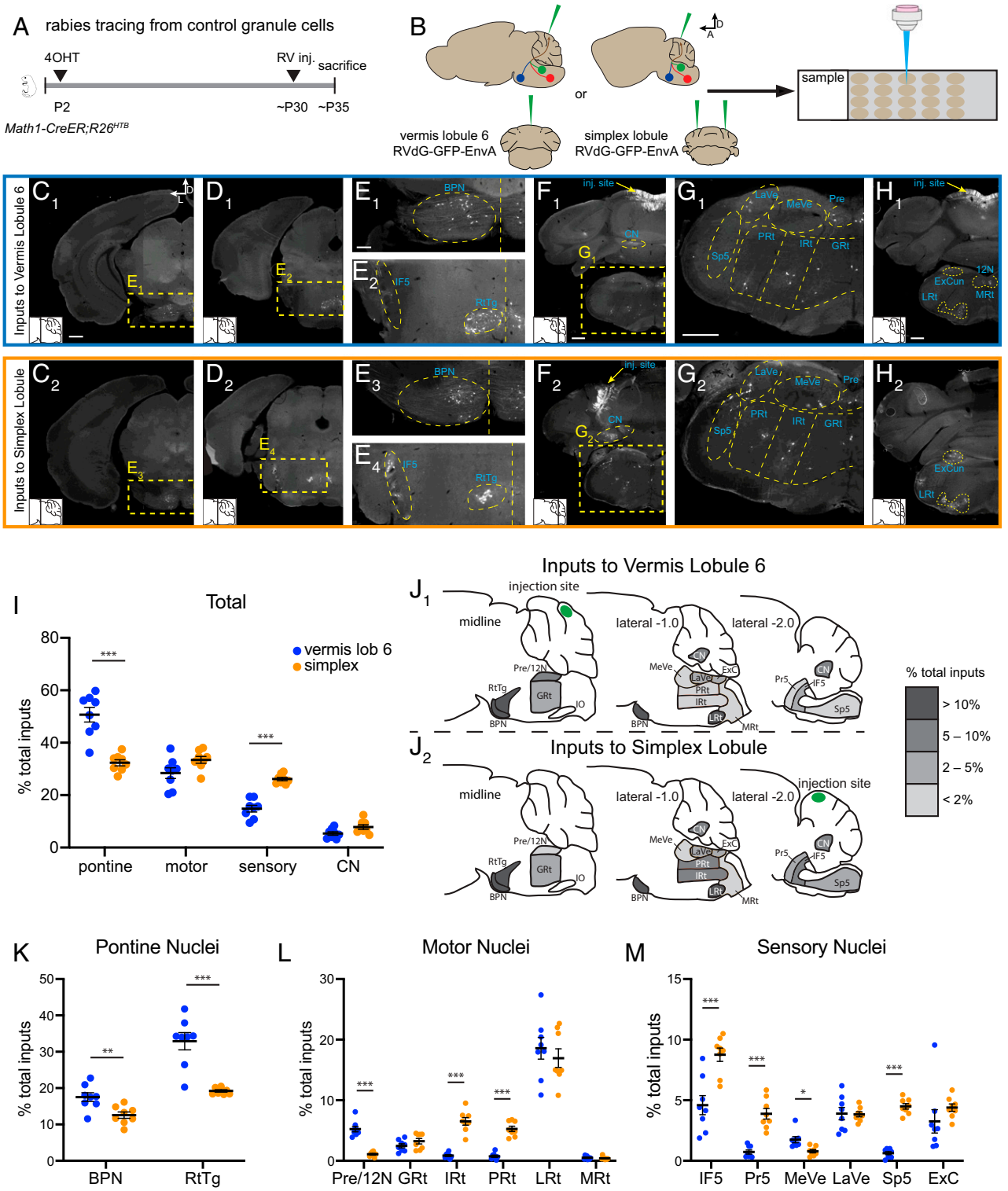

Fig. 2. Rabies tracing of mossy fiber inputs to GrCs of vermis lobule 6 and simplex. (*A* and *B*) Time course (*A*) and schematic (*B*) of retrograde monosynaptic rabies tracing. RVdG-GFP-EnvA, rabies virus deleted for glycoprotein, expressing GFP, and pseudotyped with EnvA. D, dorsal; A, anterior. *Top*, sagittal view; *Bottom*, coronal view. (*C–H*) Example stitched slide scanner images of GFP-labeled input cells to vermis lobule 6 (C_1–H_1) and simplex (C_2–H_2) GrCs. D, dorsal; L, lateral. (Scale bars, 500 μm for *C*, *D*, and *F–H*; 200 μm for *E*.) *Insets* at *Bottom Left* show section planes in sagittal atlas. (*I*) Total distribution of presynaptic inputs from supercategorized brainstem nuclei to vermis lobule 6 and simplex GrCs. (*J*) Schematic summary of distribution of presynaptic inputs from brainstem nuclei to vermis lobule 6 and simplex GrCs. (*K–M*) Distribution of inputs from brainstem pontine (*K*), motor (*L*), and sensory (*M*) nuclei to vermis lobule 6 and simplex GrCs. $n = 8$ (vermis), 8 (simplex). Error bars, SEM. $^*P < 0.05$, $^{**}P < 0.01$, $^{***}P < 0.001$ corrected (multiple unpaired *t* tests with Bonferroni correction). BPN, basal pontine nucleus; CN, cerebellar nuclei; ExC, external cuneate nucleus; GRt, gigantocellular reticular nucleus; IF5, interfascicular trigeminal nucleus; IRt, intermediate reticular nucleus; LaVe, lateral vestibular nuclei; LRt, lateral reticular nucleus; MeVe, medial vestibular nuclei; MRt, medullary reticular nucleus; Pr5, principle trigeminal sensory nucleus; Pre/12N, prepositus/hypoglossal nuclei; PRt, parvicellular reticular nucleus; RtTg, reticulotegmental nucleus of the pons; Sp5, spinal trigeminal nucleus.

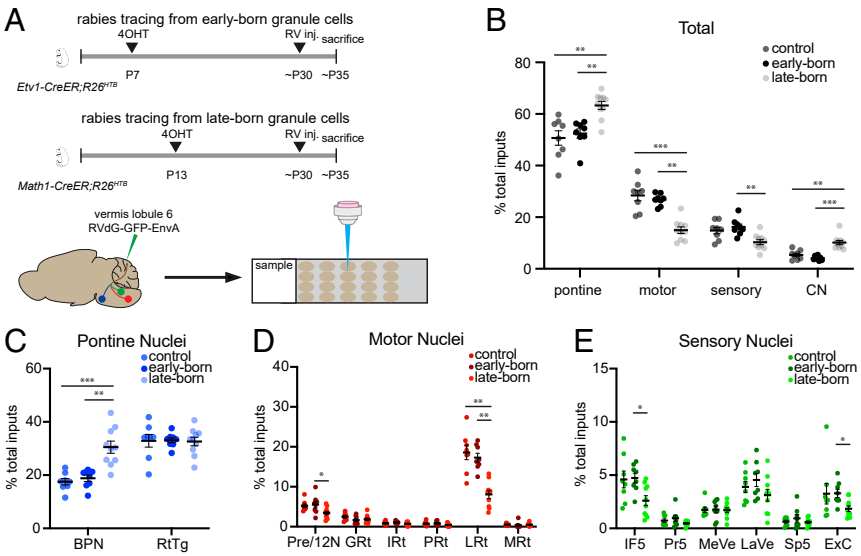

Fig. 3. Rabies tracing of mossy fiber inputs to birth-timing–defined vermis lobule 6 GrCs. (*A*) Schematic of experimental procedures; retrograde monosynaptic rabies tracing using RVdG-GFP-EnvA, rabies virus deleted for glycoprotein, expressing GFP, and pseudotyped with EnvA. (*B*) Total distribution of presynaptic inputs from supercategorized brainstem nuclei to control, early-born, and late-born GrCs of vermis lobule 6. (*C–E*) Distribution of presynaptic inputs from brainstem pontine (*C*), motor (*D*), and sensory (*E*) nuclei to control, early-born, and late-born GrCs of vermis lobule 6. $n = 8$ (control), 8 (early born), 10 (late born). Error bars, SEM. $*P < 0.05$, $**P < 0.01$, $***P < 0.001$ corrected (Kruskal–Wallis test with Dunn's multiple comparisons test). See Fig. 2 legend for anatomical abbreviations.

mice with 4OHT after P21 to drive GCaMP6f expression. We thus labeled only a sparse subset of PFs at all molecular layer depths, which facilitated imaging these thin structures with minimal signal contamination between neighboring PFs (Fig. 4*A* and *SI Appendix*, Fig. S4 *A* and *B*). We then trained water-restricted mice in an operant arm-reaching task using sucrose water as a reward, with a randomly interspersed 20% of trials ending in reward omission (10, 53). We imaged expert mice performing the operant task, followed by presentation of a stimulus panel containing visual and auditory stimuli, as well as a free reward and two aversive stimuli: orofacial air puff and tail shock; these five stimuli were repeatedly presented in a random order (Fig. 4*D* and *Materials and Methods*). We imaged at two depths in the molecular layer, manually tuning the optical apparatus to identify the superficial-most (~10 μm from the pial surface) and deepest (~10 μm from the Purkinje cell layer) imaging fields that we could access (Fig. 4*C*). This provided near-simultaneous access to Ca^{2+} activity of PFs arising from late- and early-born GrCs (Movie S1). Superficial and deep PFs had similar Ca^{2+} transient rates (*SI Appendix*, Fig. S4*C*).

We registered PFs and correlated their responses with different portions of the task and with each stimulus (Fig. 4 *E* and *F*). All results were similar when explicitly separating background from PF signals using nonnegative matrix factorization (54), consistent with our sparse labeling strategy having minimized contamination due to out-of-plane fluorescence (*SI Appendix*, Fig. S4 *D–H* and *Materials and Methods*). Furthermore, real-time compensation for axial drift and other quality-control measures allowed stable imaging across recording duration (*SI Appendix*, Fig. S4*I*). In total, we imaged five mice over 19 sessions with independent fields of view and thus recorded from 831 superficial molecular layer PFs and 511 deep molecular layer PFs from lateral vermis lobule 6 and adjacent medial simplex.

Overall, large fractions of both superficial and deep PFs exhibited responses to the operant task and free reward; smaller fractions responded to the aversive stimuli (orofacial air puff and tail shock); and even smaller fractions responded to the neutral auditory and visual stimuli (Fig. 4*G*). Both superficial and deep PFs encoded representations tiling the temporal scope of reward and reward omission trials in the operant task (Fig. 4*H*). Deep PFs, originating from early-born GrCs, were positively modulated by movement and free reward in higher proportions than superficial PFs (Fig. 4I_1 and *SI Appendix*, Fig. S5*A*); one such difference was also found in PFs negatively modulated by the task variables and stimuli (*SI Appendix*, Fig. S5 *B–D*). We also recovered PFs activated by reward, reward anticipation, and reward omission (*SI Appendix*, Fig. S5*E*) (10); the deep molecular layer had a higher proportion of reward anticipation PFs than the superficial molecular layer (Fig. 4I_2). Thus, while both superficial and deep PFs broadly represent task variables and stimuli, they do so in different proportions.

As an alternative to computing the modulation by each behavioral variable individually, we also performed linear regression analysis to determine the relative contribution of different behavioral variables to the time-varying activity of each PF (*SI Appendix*, Fig. S6*A*). This allows for concise comparison between molecular layer depths of the response to the full set of behavioral variables. We used 10 variables (premovement, postmovement, preoperant reward, postoperant reward, reward omission, free reward, air puff, tail shock, tone, and visual stimuli) to uncover which variables best explain the dynamic activity levels of each PF (*SI Appendix*, Fig. S6*B*). These analyses revealed that similar numbers of variables (regressors) contributed to activity changes in superficial and deep PFs (*SI Appendix*, Fig. S6*C*), highlighting the potential for diverse, multimodal representations in PFs at each depth. This analysis also suggested that PFs tended to respond to clusters of different but potentially related task variables and stimuli, with three main clusters representing movement, reward-related variables, and stimuli (Fig. 4*J*). There was also a weak but significant tendency for nearby PFs to have more similar regression weights (*SI Appendix*, Fig. S6*D*), consistent with a previous report (37). Because we did not monitor animals' movement, we cannot rule out similarity in responses to the various stimuli as a result of movement in response to the different stimulus events.

Evidence that Some GrCs Encode Aversion. Acquisition of the Ca^{2+} activity traces of PFs in response to diverse stimuli enabled us to investigate their encoding properties further. We found that PFs

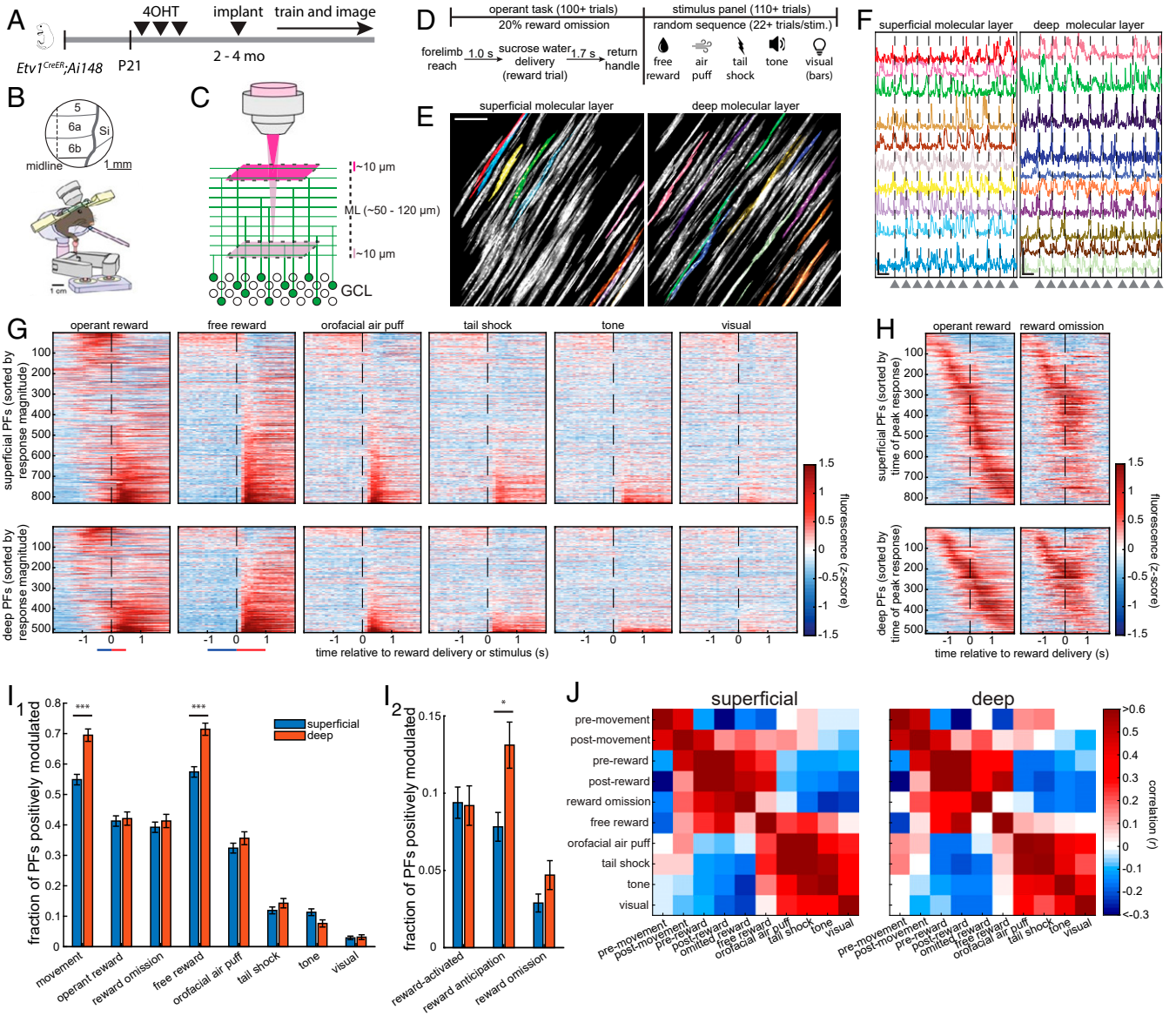

Fig. 4. Simultaneous in vivo multidepth two-photon imaging of superficial and deep parallel fibers (PFs) during an operant task and in response to a stimulus panel. (*A*) Genetic strategy for depth-unbiased GCaMP6 expression in PFs. (*B*) Window implantation. 5, vermis lobule 5; 6a/b, vermis lobule 6a/b; Si, simplex lobule. (*C*) Optical strategy for multidepth two-photon near-simultaneous imaging of superficial and deep PFs, corresponding to late- and early-born GrCs, respectively. ML, molecular layer; GCL, granule cell layer. (*D*) Operant task structure and stimulus panel with appetitive, aversive, auditory, and visual stimuli. (*E*) Example superficial and deep imaging fields of view with active PFs. (Scale bar, 40 µm.) (*F*) Example panels of PF Ca^{2+} responses from fields of view in *E* across several trials of the operant task. Gray arrowheads and vertical dashed lines denote reward onset. (Vertical scale bars, 5 SD; horizontal scale bars, 5 s.) (*G* and *H*) Heat plots of trial-averaged Ca^{2+} traces of individual PFs temporally aligned to reward delivery (*G* and *H*) or stimulus onset (*G*) and sorted by magnitude of response to operant reward or stimulus (*G*) or time of peak response during operant task trials (*H*) averaged across all trials (831 superficial and 511 deep PFs from 19 sessions from five mice). Blue and red bars show time windows used respectively in pre- and postreward/stimulus fluorescence modulation analysis. All stimulus trials were analyzed using the time windows shown under "free reward." (*I*) Fraction of PFs at both depths significantly positively modulated by each task variable or stimulus (I_1; $^{***}P < 5 \times 10^{-6}$ corrected; Wilcoxon rank-sum test with Holm–Bonferroni correction, $n = 19$ sessions), or by reward, reward anticipation, or reward omission (I_2; $^{*}P < 0.05$ corrected; Wilcoxon rank-sum test with Holm–Bonferroni correction, $n = 19$ sessions). (*J*) Linear regression analysis to explain each individual PF's time-varying fluorescence as a weighted sum of behavioral events and stimuli (*Materials and Methods*). Matrix shows the correlation coefficient between the weights assigned to each pairing of regressors across all PFs from either depth.

activated by orofacial air puff were often also activated by tail shock (Fig. 5 *A* and *B*). Comprehensive correlation analyses revealed a strong correlation between PF responses to air puff and tail shock (Fig. 5 B_1 and B_2), representing the strongest correlation between the stimuli presented (Fig. 4*J*). By contrast, there was little correlation between free reward and air puff or tail shock (Fig. 5 B_3–B_6). These trends were evident in PFs at both depths. As orofacial air puff and tail shock are unlikely to activate the same primary sensory responses, these data suggest that some GrCs could encode generalized aversive stimuli or common motor responses to aversive stimuli.

Discussion

Birth timing is a determining factor for neuronal connectivity and function in a variety of systems from insects to mammals (26). In the mammalian neocortex, for example, birth timing dictates the

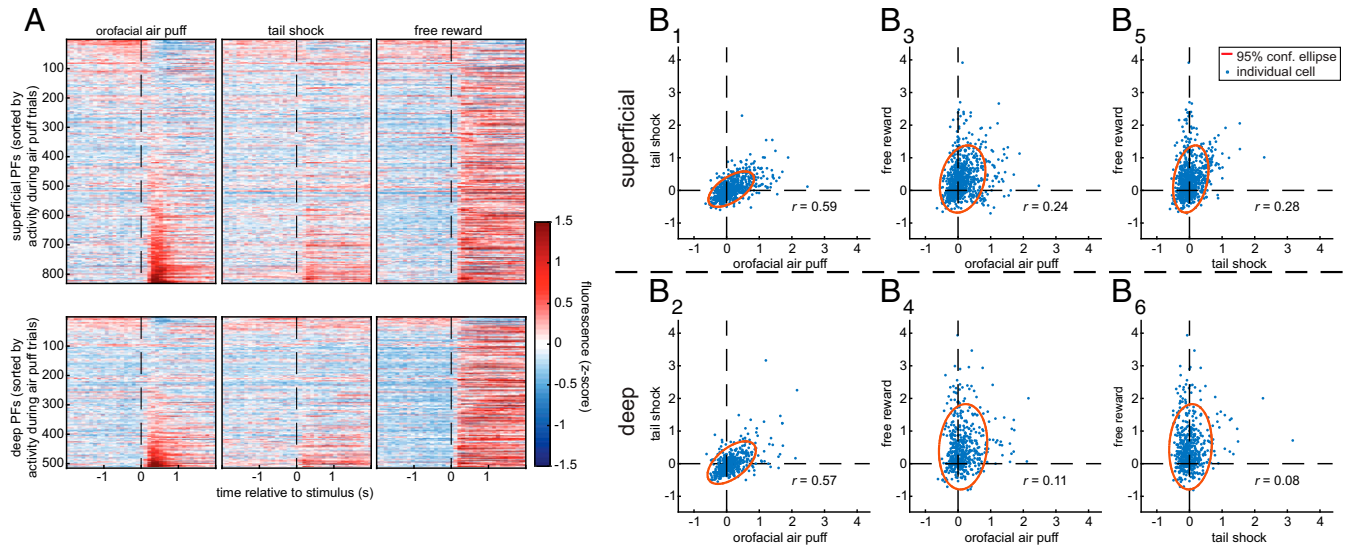

Fig. 5. Evidence for GrC encoding of aversion. (*A*) Heat plot of trial-averaged Ca^{2+} traces of individual PFs temporally aligned to air puff and tail shock and sorted by magnitude of response to air puff (831 superficial and 511 deep PFs from 19 sessions from five mice). (*B*) Following the analysis in Fig. 4*J*, for superficial (*Top*) or deep PFs (*Bottom*), correlations between the linear regression weights assigned to air puff vs. tail shock (B_1, B_2), air puff vs. free reward (B_3, B_4), and tail shock vs. free reward (B_5, B_6). Each blue dot is a PF (831 superficial PFs, 511 deep PFs), and each red ellipse denotes 95% confidence. Pearson correlation coefficients (*r*) are displayed.

cortical layers that glutamatergic excitatory neurons occupy (27, 28), which in turn predicts their connectivity patterns and functions (55). Birth timing also predicts the subtypes and cortical layers of GABAergic inhibitory neurons (56, 57) and the layer-specific axonal innervations of modulatory cholinergic neurons (30). In the cerebellar cortex, birth timing dictates the depth of the molecular layer to which the axons (PFs) of GrCs project (25). Even though PFs at different depths innervate the same Purkinje cells, whose dendrites span the entire molecular layer, there are at least two ways such spatially organized inputs could affect information processing. First, dendritic inputs at different distances from the soma can produce somatic membrane potential changes of different magnitudes and thus differentially affect action potential production (58, 59). Second, clustered synaptic inputs can summate nonlinearly to boost synaptic plasticity and transmission of synaptic potentials to the soma (58, 60–63). Thus, by mapping different mossy fiber populations to different depths of the Purkinje cell dendritic tree, GrC birth timing could modulate the impact of different inputs on cerebellar cortex output.

Our transsynaptic tracing results indicate that early- and late-born GrCs receive inputs from the same collections of brainstem nuclei (Fig. 3). Our simultaneous in vivo imaging of deep and superficial PFs—corresponding to early- and late-born GrCs—indicate that they exhibit largely similar activity patterns during an operant task and in response to a battery of stimuli (Fig. 4). These data suggest that the GrC input–output map is far from organized parallel processing, in which inputs from specific precerebellar nuclei are transmitted to specific depths of the molecular layer. Indeed, our imaging data largely agree with a recent report that did not detect differences in early- vs. late-born GrCs in their responses to sensorimotor stimuli (38). Together, these data are consistent with nonselective mossy fiber inputs onto GrCs born at different times, in line with the classic Marr–Albus framework (3, 4).

On the other hand, we identified quantitative differences between the distribution of mossy fiber inputs to early- vs. late-born GrCs, with brainstem sensory and motor nuclei contributing more inputs to early-born GrCs and pontine and cerebellar nuclei contributing more inputs to late-born GrCs. Likewise, our imaging identified small but significant differences in the proportion of GrCs positively modulated by movement, reward anticipation, and free reward. The higher proportion of deep PFs arising from early-born GrCs representing these variables coincides with a higher proportion of input from brainstem motor regions, suggesting a possible link to extracerebellar motor circuits encoding preparatory and/or reward-responsive motor activity. These data argue against a completely stochastic mossy fiber→GrC connectivity model. Future work is required to determine how differential mossy fiber inputs contribute to the differences in physiological response properties described here, and whether GrCs born at different times exhibit different activity patterns and functions in other behavioral paradigms.

The circuit architecture of the vertebrate cerebellar cortex has often been compared to that of the insect mushroom body (5, 64, 65). Both circuits feature dimensionality expansion: a small number of mossy fibers provides input to a much larger number of GrCs in the cerebellar cortex; and a small number of olfactory projection neurons (PNs) provides input to a much larger number of Kenyon cells (KCs, the intrinsic neurons of the mushroom body) for representation of different combinations of olfactory cues. Anatomical and physiological studies have provided evidence for random PN→KC connections (66–68), even though birth timing is an important determining factor for both PNs (69, 70) and KCs (71). However, other physiological studies and more recent serial electron microscopic reconstructions have uncovered aspects of connectivity that are nonrandom (65, 72–74). Specifically, a subset of axons of PNs that represent food odors converge onto individual KCs more frequently than expected from a random connectivity model; this property can be used to enhance discrimination of commonly encountered and ethologically relevant stimuli (74). Furthermore, three major KC classes born at different times from a common neuroblast receive biased input from different PN types (65). Altogether, these studies suggest that the mushroom body circuit utilizes random connectivity within local regions nested within structured organization at a larger scale (65, 74). Whether mossy fiber→GrC connectivity follows similar rules awaits future investigation.

Our study also provides insights into GrC connectivity and coding unrelated to birth timing. Our description of mossy fiber inputs to vermis lobule 6 and simplex GrCs (Fig. 2) provide profiles

of monosynaptic inputs to cerebellar GrCs. Notably, we found more pontine input to vermis lobule 6 than to simplex, a part of the cerebellar hemisphere (Fig. 2*I*). The vermis is classically considered a part of the spinocerebellar system, underscoring its reception of trigeminal and proximal somatosensory input; by contrast, the hemisphere is classically considered part of the cerebrocerebellar system, emphasizing its interconnections with the cerebral cortex via the pons (75–77). Our monosynaptic tracing results buttress the results of recent multisynaptic retrograde tracing studies from the vermis of monkeys (78), rats (79), and mice (18, 80), supporting an updated view of diverse mossy fiber inputs to vermis and hemisphere superseding the classical, dichotomous conception of mossy fiber inputs to vermis vs. hemisphere.

Recent physiological recording studies in behaving animals have highlighted the role of the cerebellum in reward processing (10–12, 81–85). Specifically, individual GrCs can encode reward delivery, omission, or expectation (10). We found that a substantial number of GrCs are activated by orofacial air puff and tail shock (Fig. 5), two aversive stimuli that use distinct sensory pathways. This finding suggests that GrCs may also encode aversion, complementing their representation of reward and expanding our understanding of the cerebellum's role in cognitive processing (13).

Materials and Methods

Mice. All procedures followed animal care and biosafety guidelines approved by Stanford University's Administrative Panel on Laboratory Animal Care and Administrative Panel of Biosafety in accordance with the NIH *Guide for the Care and Use of Laboratory Animals* (86). The day of birth was considered postnatal day 0 (P0). All mice were on CD1 and C57BL/6J mixed backgrounds. Transgenic lines *Etv1-CreER* (45), *Math1-CreER* (43), *Ai14* (46), *R26*^{HTB} (49), and *Ai148* (52) were used where indicated. Mice used to test genetic strategies were killed between P28 and P32. Mice used in anatomical experiments were injected with rabies virus between P28 and P33 and perfused 5 d later. Mice used in imaging experiments were implanted with imaging windows at between 10 and 14 wk of age. Both males and females were used in anatomical experiments; females were used in imaging experiments due to their availability. Mice were housed in plastic cages with disposable bedding on a 12-h light/dark cycle with food and water available ad libitum until placed on water restriction.

4OHT Production and Injection. 4OHT was prepared by dissolving in Chen oil (87). *Math1-CreER;Ai14* and *Math1-CreER;ROSA26*^{HTB} pups were injected intraperitoneally at P2 (50 mg/kg) or P13 (150 mg/kg). P13 *Etv1-CreER;Ai14* or *Etv1-CreER;ROSA26*^{HTB} pups were injected intraperitoneally at P7 with 50 to 150 mg/kg 4OHT. *Etv1-CreER;Ai148* mice used in imaging experiments were injected intraperitoneally after P21 two to five times with 150 mg/kg 4OHT.

Immunostaining. Mice were deeply anesthetized using 2.5% Avertin and perfused transcardially, first with ∼10 mL phosphate-buffered saline (PBS) then ∼25 mL 4% paraformaldehyde (PFA) in PBS. The fixed brains were dissected out and postfixed overnight at 4 °C in 4% PFA in PBS. Brains were then immersed in sucrose for 24 to 48 h, embedded in optimum cutting temperature (OCT, Tissue Tek), and sectioned on a cryostat (Leica).

For genetic strategy proof-of-principle experiments, 40-μm sections of the cerebellar vermis were collected in PBS, washed twice in PBS for 10 min, incubated in 10% normal donkey serum (NDS) in PBST (PBS with 0.3% Triton X-100) for 2 h at room temperature, and incubated in primary antibody (1:1,000 mouse anti-calbindin, Sigma; 1:500 rabbit anti-DsRed, Clontech; 1:1,000 guinea pig anti-vGluT1, Millipore) solution containing 5% NDS in PBST for two overnights at 4 °C. Sections were then washed three times in PBST, each for 10 min; incubated in primary antibody solution containing 5% NDS in PBST for 2 h at room temperature; washed in PBST for 10 min; incubated in PBST with DAPI (1:10,000 of 5 mg/mL, Sigma-Aldrich) for 30 min; and then successively washed in PBST and PBS, each for 10 min. Sections were then mounted on Superfrost Plus slides, coverslipped with Fluoromount-G, and allowed to dry for at least 4 h at room temperature before imaging.

For rabies tracing experiments, 60-μm sections encompassing the entire hindbrain (from AP −3.5 to −8.5 to bregma) were collected onto Superfrost Plus slides in the order of sectioning. Slides were dried at room temperature overnight before further processing. Following overnight drying, slides were washed in PBST (PBS with 0.3% Triton X-100) for 10 min, incubated in PBST with DAPI (1:10,000 of 5 mg/mL, Sigma-Aldrich) for 30 min, then washed once in PBST and once in PBS, each for 10 min (all steps at room temperature). Slides were then dried and coverslipped with Fluoromount-G (Thermo Fisher Scientific). Slides were allowed to dry for at least 4 h at room temperature before slide scanner imaging. Whole slides were then imaged with a 10× objective using a Leica Ariol slide scanner and a SL200 slide loader. Images were stitched together and viewed using Leica's Ariol ImageScope program.

Fluorescence Imaging. Images were taken on a Zeiss LSM 780 laser-scanning confocal microscope (Carl Zeiss). To quantify the portion of the molecular layer innervated by genetically labeled GrCs, fluorescence intensity measurements were taken on unprocessed images in Fiji (ImageJ), and data were processed using custom MATLAB scripts. A 400-pixel-wide segmented line was drawn from the border of the deep molecular layer to the pial surface (the border of the superficial molecular layer), as defined by counterstains with calbindin and vGluT1, and average intensity values along the line were measured using the Plot Profile command. The intensity traces were interpolated into 100 bins from deep to superficial using custom code (MATLAB), and the traces from individual sections were normalized to a maximum of 100. Twelve sections were collected from two mice of the early-born, late-born, and control cohorts.

Rabies Virus Production and Injection. Pseudotyped (EnvA-coated) G-deleted RV encoding expression of eGFP were produced following a published protocol (88). Mice were anesthetized with 1.5 to 2.0% isoflurane and placed in a stereotaxic apparatus (Kopf Instruments). The following sets of coordinates (in millimeters) were used: 0.0 AP, 0.0 ML, −0.3 DV and 0.5 AP, 0.0 ML, −0.3 DV (relative to the posterior suture; or −3.2 and −3.7 AP to lambda) for injections targeted to vermis lobule 6; and −2.0 AP, ±2.0 ML, −0.3 DV (relative to lambda) for injections targeted to bilateral simplex. For injections targeting control GrCs in vermis lobule 6 and simplex (Fig. 2), 100 nL RVdG-eGFP-EnvA was injected into each site. For injections targeting early- and late-born GrCs in vermis lobule 6 (Fig. 3), 300 nL RVdG-eGFP-EnvA was injected into each site. Following injection, mice were housed in a biosafety level 2 (BSL2) facility to allow for rabies transsynaptic spread and eGFP expression. All mice were injected between postnatal days 28 and 33 and killed 5 d after RV injection.

Quantification of Rabies Tracing Results. Quantification of brainstem subregions relied on boundaries outlined in a mouse brain atlas (89). Anatomically contiguous regions with similar functions and lacking clear-cut anatomical boundaries were combined. For example, the prepositus (Pre) and hypoglossal nuclei (12N) were combined due to their anatomical continuity, a lack of distinguishing anatomical markers in our histological preparation, and their coinvolvement in motor coordination of facial muscles. The parvicellular reticular nucleus (PCRt) and its alpha part (PCRtA) were combined into PRt (parvicellular reticular nucleus); the intermediate reticular nucleus (IRt) and its alpha part (IRtA) were combined into IRt (intermediate reticular nucleus); the gigantocellular nucleus (Gi), including its alpha (GiA) and ventral (GiV) parts, and the lateral (LPGi) and dorsal (DPGi) paragigantocellular nuclei were combined into GRt (gigantocellular reticular nucleus); the dorsal (MdD) and ventral (MdV) parts of the medullary reticular nuclei were combined into MRt (medullary reticular nucleus). The magnocellular (MVeMC) and parvicellular (MVePC) parts of the vestibular nuclei and the vestibulocerebellar nucleus (VeCb) were combined into MeVe (medial vestibular nucleus); while the lateral (LVe), spinal (SpVe), and superior (SuVe) vestibular subnuclei were combined into LaVe (lateral vestibular nucleus). The dorsomedial (Pr5DL) and ventrolateral (Pr5VL) parts of the principal sensory trigeminal nucleus were combined into Pr5 (principal sensory trigeminal nucleus); and the oral (Sp5O), dorsomedial (DMSp5), interpolar (Sp5I), and caudal (Sp5C) parts of the spinal trigeminal nucleus were combined into Sp5 (spinal trigeminal nucleus). Regions contributing under 0.75% total input, including the spinal cord, nucleus of the facial nerve (7N), dorsal cochlear nucleus (DC), and inferior olive (IO) were not included in the final analysis due to the very low number of labeled cells in these regions. As *ROSA26*^{HTB} mice express histone-GFP in potential starter cells (46), and our rabies virus also expressed GFP, we could not distinguish starter cells from local presynaptic inputs. Our analysis thus focused on distant inputs to GrCs. We did not quantify local unipolar brush cell inputs to GrCs.

Tracing Statistics. Unpaired *t* tests with Bonferroni corrections and Kruskal–Wallis tests with Dunn's multiple comparisons tests were performed using Prism 9 (GraphPad).

Window Implantation. Surgeries were performed as described previously (10). Mice were anesthetized using isoflurane (1.25 to 2.5% in 0.7 to 1.3 L per minute of O_2) during surgeries. Hair was removed from a small patch of skin, skin was cleaned, and an incision was made to remove the patch of skin. Connective tissue and muscle were then peeled back, and the skull was dried. A 3-mm-diameter cranial window centered rostrocaudally over the postlambda suture and 1.5 mm right of the midline was then exposed via drilling, positioning the window over cerebellar lobules 6 and medial simplex. To seal the skull opening, a #0 3-mm-diameter glass coverslip (Warner Instruments) was affixed to the bottom of a 3-mm-outer-diameter, 2.7-mm-inner-diameter stainless steel tube (McMaster) cut to 1-mm height. The glass/tube combination was stereotaxically inserted into the opening in the skull at an angle of 45° from the vertical axis and 25° from the AP axis. The window was then fixed in place and sealed with Metabond (Parkell). Next, a custom stainless steel head fixation plate was fixed to the skull with Metabond and dental cement (Coltene Whaledent). The 1.2-mm-thickness fixation plate had a 5-mm opening to accommodate the stainless steel tube protruding from the window, and two lateral extensions to permit fixing the plate to stainless steel holding bars during imaging and behavior.

Operant Task. Mice were trained as described previously (10). During water restriction, mice were monitored daily for signs of distress, coat quality, eye closing, hunching, and lethargy to ensure adequate water intake. Following 2 d of water restriction, mice were trained for 10 to 14 d for about 20 to 60 min daily, depending on performance and satiety. Mice were first trained with reward trials only, then with reward withheld on a random, but never consecutive, 20% of trials (reward omission). In both tasks, we recorded licking at 200 Hz using a capacitive sensor coupled to the metal water port, which delivered approximately ∼6 μL 4% sucrose water reward near the animal's mouth. During training and in all experiments, mice were head fixed, with their bodies from the torso down in a custom printed optically transparent plastic tube. Mice learned to voluntarily initiate pushing the handle of a manipulandum. The robot constrained movement of the manipulandum to the forward axis. Handle position was controlled and monitored by two motors and encoders (Maxon B7A1F24007CF, containing DCX22S EB KL 24V motor with ENX 16 RIO 65536IMP encoder), and robotic control relied on nested feedback loops in a field-programmable gate array (10 kHz) and a real-time operating system computer (1 kHz), both in a National Instruments cRIO chassis, as well as a Windows PC (200 Hz). The controllers were programmed in LabVIEW and permitted precise robotic positioning and application of forces to the handle with a 1-kHz bandwidth to restrict motion as needed (53). The device recorded the handle position with a 200-Hz sampling rate and encoder resolution of 0.003 mm and permitted linear movements of a maximum length of 8 mm, after which the trial terminated. Following a delay (1 s), a solenoid delivered the water reward. Following another delay (1.7 s), the handle began to return to the home position. This process took 2 s to complete, after which the mouse could initiate the next movement at any time. During reward omission trials, reward was withheld on a randomly interspersed 20% of trials, but never on two consecutive trials.

Stimulus Panel. A stimulus panel including delivery of free reward, orofacial air puff, tail shock, sliding tone, and visual stimulus was designed. A total of 110 to 120 stimuli were presented over 15.4 min, with equal time intervals between presentation of successive stimuli. Free rewards consisted of a water reward of the same size as those of the operant task. Orofacial air puffs aimed at the mouse's left whisker pad and eye were triggered through an external custom-built stimulus delivery system; air puffs were tested before imaging and always elicited eyeblink. Tail shocks were administered via an electrical stimulator (model #A320D, World Precision Instruments); electrode gel (Spectra 360, Parker Laboratories) was placed on the tail and the positive and negative leads (18-ga copper wire) were securely taped onto the middle portion of the tail 1 cm apart, and a 5-V pulse to the stimulator triggered delivery of an electrical current (5 mA, 2 s). The auditory tone stimulus consisted of a WAV file encoding a 2-s-long tone rising from 1 kHz to 20 kHz and then back down to 1 kHz and was delivered via speakers from 1 m away from the mouse. The visual stimulus consisted of a 1-s-duration moving vertical bar of blue light on a custom-built LED grid (Sparkfun WS2812B).

Imaging and Optics. All Ca^{2+} imaging was performed using a 40× 0.8 numerical aperture (NA) objective (LUMPlanFLN-W, Olympus) and a custom two-photon microscope with an articulating objective arm. A 920-nm laser excitation was delivered to the sample from a Ti:sapphire laser (MaiTai, Spectra Physics) at powers of around 40 and 50 mW at the superficial and deep imaging depths, respectively. ScanImage software (Vidrio Technologies) was used to control all image acquisition hardware. To image the superficial and deep molecular layer together, suitable depths for each were first identified. A z-piezo (P-725.4CD, Physik Instrumente) was used to lower the focal plane just below the pial surface until a full-field plane of the molecular layer was visualizable; this plane was recorded as the superficial depth. A full-field plane of the molecular layer just above the Purkinje cell layer (40 to 100 μm below the superficial field of view) was then focused to and recorded as the deep depth. During imaging, ScanImage interleaved frame acquisitions at each depth by moving the z-piezo between frames, yielding a volume acquisition rate of 9.75 Hz. At each depth, resonant galvanometers scanned a 240 × 240–μm field of view. To ensure alignment of the articulating objective to the glass window on the brain, a back-reflection procedure was performed. A low power visible red laser (CPS180, ThorLabs), coaligned to the infrared beam onto the glass window, was projected into the cerebellar window; the red back reflection was then viewed via an iris placed on the objective port. The mouse and objective angles were positioned to center the back reflection into the iris aperture. To align imaging data to behavioral data, the behavioral computer acquired the microscope's frame clock signal simultaneously with each mouse's behavioral data.

Image Processing. Files containing both superficial and deep images were first split by depth. Normcorre image registration software corrected rigid and piecewise nonrigid lateral brain motion (90). Downsampled videos were manually inspected, and imaging sessions with significant brain motion/depth shift were discarded. Individual active PFs were identified in our imaging videos using automated cell sorting based on principal and independent component analyses (PCA/ICA). PFs corresponded to a weighted sum of pixels forming a spatial filter. Automated and manual segmentation and thresholding were used to truncate these filters down to individual PFs by eliminating spurious, disconnected components. Each PF's time-varying fluorescence trace was extracted by applying the spatial filter to the processed videos. Slow drift was removed from each trace by subtracting a 10th-percentile–filtered (15-s sliding window) version of the signal. Finally, each PF's fluorescence trace was z scored to correct for differences in brightness between PFs; all fluorescence values were then reported in SD units. Data were aligned to the time of reward or stimulus delivery. For reward omission trials, data were aligned to the time at which reward would have been delivered following movement termination. The aligned fluorescence response of each PF was averaged across trials to produce the triggered averages shown.

Modulation Analysis. Time windows for modulation analysis were defined with reward (or, for reward omission trials, when reward would have been delivered) or stimulus delivery timepoints serving as timepoint 0.0 s. To determine whether a PF was significantly modulated by a task variable/stimulus, we compared fluorescence before and after stimulus/variable. For each operant trial, we computed fluorescence for each cell averaged over the two time windows [0.0, 0.5] s and [−0.5, 0.0] s, while for each stimulus delivery we used the time windows [−1.0, 0.0] s and [0, 1.0] s. We then compared fluorescence in the two time windows. Significance for each cell was determined using a cutoff of $P = 0.05$.

For the operant task, we defined reward-activated PFs as those whose fluorescence was significantly greater after than before reward, and significantly greater after reward than after reward omission ($P < 0.05$ for both comparisons). We defined reward anticipation PFs as those whose fluorescence was significantly greater after reward omission than after reward, and significantly greater just prior to reward than prior to movement ($P < 0.05$ for both comparisons). We defined reward omission PFs as those whose fluorescence was significantly greater after reward omissions than after reward ($P < 0.05$), excluding those previously defined as reward anticipation PFs. In analysis of these three PF response types, pre- and posttime windows were taken to be [0.0, 0.5] s and [−0.5, 0.0] s.

To confirm that observed negative modulations were not z-plane motion artifacts, we also performed this analysis on nonnegative source signals demixed from putative background fluorescence (see *SI Appendix*), which exclude negative fluorescence transients, and found the same number of negatively modulated PFs. Similarly, computing modulations using event rates rather than fluorescence traces yielded substantial numbers of negatively modulated PFs, together suggesting that these reflect reduced probability of activation of these cells at the corresponding times, rather than brain motion.

Regression Analysis. To determine which task variables/stimuli predict PF activity, we used linear regression analysis to reproduce the time-varying fluorescence of each individual cell as a weighted sum of boxcar "indicator" functions

corresponding to each behavioral variable of interest. The operant regressors corresponding to premovement, postmovement, prereward, and postreward used boxcars of width 0.5 s just prior or subsequent to either movement or reward. The regressor corresponding to operant reward omission used a boxcar in the later period, [0.5, 1.5] s with respect to reward omission. The regressors corresponding to the stimuli—free reward, air puff, tail shock, tone, and visual—used boxcars at [0, 1] s with respect to stimulus onset. Finally, to account for the Ca^{2+} indicator kinetics, we convolved these indicators with a 150-ms decaying exponential.

Using these regressors, we then fit a linear regression model. We first used a 10-fold cross-validated least absolute shrinkage and selection operator (LASSO) penalized regularization. For each cell, we determined the LASSO penalty corresponding to the best cross-validated model fit (minimum cross-validated model deviance) and identified the corresponding set of regressors with nonzero weights. We then fit a linear regression model using only that minimal set of regressors, defined as significant if $P < 0.01$. Similar results were obtained when fitting the regression model to binarized event rasters rather than raw fluorescence traces, although these models typically included fewer regressors overall. To further confirm that our models did not overfit the data, we also performed this procedure on two halves of the data separately, and the resulting regression coefficients were correlated at $r = 0.87 \pm 0.01$ and 0.88 ± 0.01 in superficial and deep PFs, suggesting a high degree of consistency.

The choice of regressors and linear regression model were meant to be the simplest and most interpretable way to compare response properties at the two imaging depths, rather than to provide the most accurate reconstruction of single-cell fluorescence changes. In particular, the regressors only tiled a relatively small subset of the experimental time course and were limited in number. The regression outputs were thus correlated with the full time series of individual cells at only $r = 0.19 \pm 0.004$ and 0.22 ± 0.005 in superficial and deep molecular layer, respectively.

Imaging Statistics. MATLAB (Mathworks) was used for all statistical tests. All comparisons of unpaired means of two groups used Wilcoxon rank-sum tests. All comparisons of paired means of two groups used Wilcoxon signed-rank tests. *P* values were adjusted using the Holm–Bonferroni multiple comparisons correction.

Data Availability. All study data are included in the article and/or supporting information. Reagents and code are available upon reasonable request to the corresponding author.

ACKNOWLEDGMENTS. We thank the L.L. laboratory, especially H. Li, J. Lui, and Y. Takeo, for feedback on the project and comments on the manuscript; M. Molacavage for administrative assistance; C. Manalac for assistance with genotyping; and A. Joyner for the *Math1-CreER* mice and M. Goulding for *R26*^{HTB} mice. S.A.S. was supported by an NSF Graduate Research Fellowship and a Regina Casper Stanford Graduate Fellowship. M.J.W. was supported by a Career Award at the Scientific Interface from the Burroughs Wellcome Fund. N.P-D. was supported by the Biology Summer Undergraduate Research Program and an Undergraduate Advising and Research Major Grant. K.T.B. was supported by the Brain and Behavior Research Foundation (NARSAD 26845). L.L. is an investigator of the Howard Hughes Medical Institute. This work was supported by NIH grants K99-DA041445 (to K.T.B.) and R01-NS080835 (to L.L.).

1. W. Lange, Cell number and cell density in the cerebellar cortex of man and some other mammals. *Cell Tissue Res.* **157**, 115–124 (1975).
2. S. Herculano-Houzel, Coordinated scaling of cortical and cerebellar numbers of neurons. *Front. Neuroanat.* **4**, 12 (2010).
3. D. Marr, A theory of cerebellar cortex. *J. Physiol.* **202**, 437–470 (1969).
4. J. S. Albus, A theory of cerebellar function. *Math. Biosci.* **10**, 25–61 (1971).
5. A. Litwin-Kumar, K. D. Harris, R. Axel, H. Sompolinsky, L. F. Abbott, Optimal degrees of synaptic connectivity. *Neuron* **93**, 1153–1164.e7 (2017).
6. N. B. Sawtell, Multimodal integration in granule cells as a basis for associative plasticity and sensory prediction in a cerebellum-like circuit. *Neuron* **66**, 573–584 (2010).
7. C.-C. Huang *et al*., Convergence of pontine and proprioceptive streams onto multimodal cerebellar granule cells. *eLife* **2**, e00400 (2013).
8. T. Ishikawa, M. Shimuta, M. Häusser, Multimodal sensory integration in single cerebellar granule cells in vivo. *eLife* **4**, e12916 (2015).
9. F. P. Chabrol, A. Arenz, M. T. Wiechert, T. W. Margrie, D. A. DiGregorio, Synaptic diversity enables temporal coding of coincident multisensory inputs in single neurons. *Nat. Neurosci.* **18**, 718–727 (2015).
10. M. J. Wagner, T. H. Kim, J. Savall, M. J. Schnitzer, L. Luo, Cerebellar granule cells encode the expectation of reward. *Nature* **544**, 96–100 (2017).
11. A. Giovannucci *et al*., Cerebellar granule cells acquire a widespread predictive feedback signal during motor learning. *Nat. Neurosci.* **20**, 727–734 (2017).
12. M. I. Becker, A. L. Person, Cerebellar granule cells expand their talents. *Nat. Neurosci.* **20**, 633–634 (2017).
13. M. J. Wagner, L. Luo, Neocortex-cerebellum circuits for cognitive processing. *Trends Neurosci.* **43**, 42–54 (2020).
14. A. Badura, C. I. De Zeeuw, Cerebellar granule cells: Dense, rich and evolving representations. *Curr. Biol.* **27**, R415–R418 (2017).
15. J. I. Gilmer, A. L. Person, Morphological constraints on cerebellar granule cell combinatorial diversity. *J. Neurosci.* **37**, 12153–12166 (2017).
16. L. D. Knogler, D. A. Markov, E. I. Dragomir, V. Štih, R. Portugues, Sensorimotor representations in cerebellar granule cells in larval zebrafish are dense, spatially organized, and non-temporally patterned. *Curr. Biol.* **27**, 1288–1302 (2017).
17. J. I. Gilmer, A. L. Person, Theoretically sparse, empirically dense: New views on cerebellar granule cells. *Trends Neurosci.* **41**, 874–877 (2018).
18. M. J. Wagner *et al*., Shared cortex-cerebellum dynamics in the execution and learning of a motor task. *Cell* **177**, 669–682.e24 (2019).
19. R. A. Carter *et al*., A single-cell transcriptional atlas of the developing murine cerebellum. *Curr. Biol.* **28**, 2910–2920.e2 (2018).
20. I. Gupta *et al*., Single-cell isoform RNA sequencing characterizes isoforms in thousands of cerebellar cells. *Nat. Biotechnol.*, 10.1038/nbt.4259 (2018).
21. A. B. Rosenberg *et al*., Single-cell profiling of the developing mouse brain and spinal cord with split-pool barcoding. *Science* **360**, 176–182 (2018).
22. V. Kozareva *et al*., A transcriptomic atlas of the mouse cerebellum reveals regional specializations and novel cell types *bioRxiv* [Preprint] (2020). https://doi.org/10.1101/2020.03.04.976407 (Accessed 28 January 2021).
23. G. G. Consalez, D. Goldowitz, F. Casoni, R. Hawkes, Origins, development, and compartmentation of the granule cells of the cerebellum. *Front. Neural Circuits* **14**, 611841 (2021).
24. H. Zong, J. S. Espinosa, H. H. Su, M. D. Muzumdar, L. Luo, Mosaic analysis with double markers in mice. *Cell* **121**, 479–492 (2005).
25. J. S. Espinosa, L. Luo, Timing neurogenesis and differentiation: Insights from quantitative clonal analyses of cerebellar granule cells. *J. Neurosci.* **28**, 2301–2312 (2008).
26. H. Li, S. A. Shuster, J. Li, L. Luo, Linking neuronal lineage and wiring specificity. *Neural Dev.* **13**, 5 (2018).
27. J. B. Angevine Jr, R. L. Sidman, Autoradiographic study of cell migration during histogenesis of cerebral cortex in the mouse. *Nature* **192**, 766–768 (1961).
28. B. J. Molyneaux, P. Arlotta, J. R. L. Menezes, J. D. Macklis, Neuronal subtype specification in the cerebral cortex. *Nat. Rev. Neurosci.* **8**, 427–437 (2007).
29. Y. Deguchi, F. Donato, I. Galimberti, E. Cabuy, P. Caroni, Temporally matched subpopulations of selectively interconnected principal neurons in the hippocampus. *Nat. Neurosci.* **14**, 495–504 (2011).
30. K. C. Allaway *et al*., Cellular birthdate predicts laminar and regional cholinergic projection topography in the forebrain. *eLife* **9**, e63249 (2020).
31. F. Imamura, A. E. Ayoub, P. Rakic, C. A. Greer, Timing of neurogenesis is a determinant of olfactory circuitry. *Nat. Neurosci.* **14**, 331–337 (2011).
32. F. Imamura, C. A. Greer, Segregated labeling of olfactory bulb projection neurons based on their birthdates. *Eur. J. Neurosci.* **41**, 147–156 (2015).
33. U. Chon, B. J. LaFever, U. Nguyen, Y. Kim, F. Imamura, Topographically distinct projection patterns of early-generated and late-generated projection neurons in the mouse olfactory bulb. *eNeuro*, 10.1523/ENEURO.0369-20.2020 (2020).
34. M. Tripodi, A. E. Stepien, S. Arber, Motor antagonism exposed by spatial segregation and timing of neurogenesis. *Nature* **479**, 61–66 (2011).
35. M. Tripodi, S. Arber, Regulation of motor circuit assembly by spatial and temporal mechanisms. *Curr. Opin. Neurobiol.* **22**, 615–623 (2012).
36. L. J. Pellegrino, J. Altman, Effects of differential interference with postnatal cerebellar neurogenesis on motor performance, activity level, and maze learning of rats: A developmental study. *J. Comp. Physiol. Psychol.* **93**, 1–33 (1979).
37. C. D. Wilms, M. Häusser, Reading out a spatiotemporal population code by imaging neighbouring parallel fibre axons in vivo. *Nat. Commun.* **6**, 6464 (2015).
38. K. H. Markwalter, Y. Yang, T. E. Holy, A. Bonni, Sensorimotor coding of vermal granule neurons in the developing mammalian cerebellum. *J. Neurosci.* **39**, 6626–6643 (2019).
39. K. Leto *et al*., Consensus paper: Cerebellar development. *Cerebellum* **15**, 789–828 (2016).
40. C. A. Mason, E. Gregory, Postnatal maturation of cerebellar mossy and climbing fibers: Transient expression of dual features on single axons. *J. Neurosci.* **4**, 1715–1735 (1984).
41. J. Altman, Postnatal development of the cerebellar cortex in the rat. I. The external germinal layer and the transitional molecular layer. *J. Comp. Neurol.* **145**, 353–397 (1972).
42. E. S. Lein *et al*., Genome-wide atlas of gene expression in the adult mouse brain. *Nature* **445**, 168–176 (2007).
43. R. Machold, G. Fishell, Math1 is expressed in temporally discrete pools of cerebellar rhombic-lip neural progenitors. *Neuron* **48**, 17–24 (2005).
44. N. Ben-Arie *et al*., Math1 is essential for genesis of cerebellar granule neurons. *Nature* **390**, 169–172 (1997).
45. H. Taniguchi *et al*., A resource of Cre driver lines for genetic targeting of GABAergic neurons in cerebral cortex. *Neuron* **71**, 995–1013 (2011). Corrected in: *Neuron*. **72**, 1091 (2011).
46. L. Madisen *et al*., A robust and high-throughput Cre reporting and characterization system for the whole mouse brain. *Nat. Neurosci.* **13**, 133–140 (2010).

47. I. R. Wickersham, S. Finke, K.-K. Conzelmann, E. M. Callaway, Retrograde neuronal tracing with a deletion-mutant rabies virus. *Nat. Methods* **4**, 47–49 (2007).
48. E. M. Callaway, L. Luo, Monosynaptic circuit tracing with glycoprotein-deleted rabies viruses. *J. Neurosci.* **35**, 8979–8985 (2015).
49. Y. Li *et al*., Molecular layer perforant path-associated cells contribute to feed-forward inhibition in the adult dentate gyrus. *Proc. Natl. Acad. Sci. U.S.A.* **110**, 9106–9111 (2013).
50. R. R. Llinás, K. D. Walton, E. J. Lang, "Cerebellum" in *The Synaptic Organization of the Brain*, G. M. Shepherd, Ed. (Oxford University Press, 2004), pp. 271–310.
51. Y. Fu, P. Tvrdik, N. Makki, G. Paxinos, C. Watson, Precerebellar cell groups in the hindbrain of the mouse defined by retrograde tracing and correlated with cumulative Wnt1-cre genetic labeling. *Cerebellum* **10**, 570–584 (2011).
52. T. L. Daigle *et al*., A suite of transgenic driver and reporter mouse lines with enhanced brain-cell-type targeting and functionality. *Cell* **174**, 465–480.e22 (2018).
53. M. J. Wagner, J. Savall, T. H. Kim, M. J. Schnitzer, L. Luo, Skilled reaching tasks for head-fixed mice using a robotic manipulandum. *Nat. Protoc.* **15**, 1237–1254 (2020).
54. S. W. Keemink *et al*., FISSA: A neuropil decontamination toolbox for calcium imaging signals. *Sci. Rep.* **8**, 3493 (2018).
55. R. J. Douglas, K. A. C. Martin, Neuronal circuits of the neocortex. *Annu. Rev. Neurosci.* **27**, 419–451 (2004).
56. G. Miyoshi, S. J. B. Butt, H. Takebayashi, G. Fishell, Physiologically distinct temporal cohorts of cortical interneurons arise from telencephalic Olig2-expressing precursors. *J. Neurosci.* **27**, 7786–7798 (2007).
57. H. Taniguchi, J. Lu, Z. J. Huang, The spatial and temporal origin of chandelier cells in mouse neocortex. *Science* **339**, 70–74 (2013).
58. G. Stuart, N. Spruston, M. Häusser, *Dendrites* (Oxford University Press, 2016).
59. E. De Schutter, J. M. Bower, Simulated responses of cerebellar Purkinje cells are independent of the dendritic location of granule cell synaptic inputs. *Proc. Natl. Acad. Sci. U.S.A.* **91**, 4736–4740 (1994).
60. S. S. Wang, W. Denk, M. Häusser, Coincidence detection in single dendritic spines mediated by calcium release. *Nat. Neurosci.* **3**, 1266–1273 (2000).
61. P. Marcaggi, D. Attwell, Endocannabinoid signaling depends on the spatial pattern of synapse activation. *Nat. Neurosci.* **8**, 776–781 (2005).
62. E. A. Rancz, M. Häusser, Dendritic calcium spikes are tunable triggers of cannabinoid release and short-term synaptic plasticity in cerebellar Purkinje neurons. *J. Neurosci.* **26**, 5428–5437 (2006).
63. N. Takahashi *et al*., Locally synchronized synaptic inputs. *Science* **335**, 353–356 (2012).
64. C. F. Stevens, What the fly's nose tells the fly's brain. *Proc. Natl. Acad. Sci. U.S.A.* **112**, 9460–9465 (2015).
65. F. Li *et al*., The connectome of the adult Drosophila mushroom body provides insights into function. *eLife* **9**, e62576 (2020).
66. L. M. Masuda-Nakagawa, N. K. Tanaka, C. J. O'Kane, Stereotypic and random patterns of connectivity in the larval mushroom body calyx of Drosophila. *Proc. Natl. Acad. Sci. U.S.A.* **102**, 19027–19032 (2005).
67. M. Murthy, I. Fiete, G. Laurent, Testing odor response stereotypy in the Drosophila mushroom body. *Neuron* **59**, 1009–1023 (2008).
68. S. J. C. Caron, V. Ruta, L. F. Abbott, R. Axel, Random convergence of olfactory inputs in the Drosophila mushroom body. *Nature* **497**, 113–117 (2013).
69. G. S. Jefferis, E. C. Marin, R. F. Stocker, L. Luo, Target neuron prespecification in the olfactory map of Drosophila. *Nature* **414**, 204–208 (2001).
70. H.-H. Yu *et al*., A complete developmental sequence of a Drosophila neuronal lineage as revealed by twin-spot MARCM. *PLoS Biol.* **8**, e1000461 (2010).
71. T. Lee, A. Lee, L. Luo, Development of the Drosophila mushroom bodies: Sequential generation of three distinct types of neurons from a neuroblast. *Development* **126**, 4065–4076 (1999).
72. E. Gruntman, G. C. Turner, Integration of the olfactory code across dendritic claws of single mushroom body neurons. *Nat. Neurosci.* **16**, 1821–1829 (2013).
73. Z. Zheng *et al*., A complete electron microscopy volume of the brain of adult Drosophila melanogaster. *Cell* **174**, 730–743.e22 (2018).
74. Z. Zheng *et al*., Structured sampling of olfactory input by the fly mushroom body *bioRxiv* [Preprint] (2020). https://doi.org/10.1101/2020.04.17.047167 (Accessed 28 January 2021).
75. J. Jansen, A. Brodal, Experimental studies on the intrinsic fibers of the cerebellum. II. The cortico-nuclear projection. *J. Comp. Neurol.* **73**, 267–321 (1940).
76. W. W. Chambers, J. M. Sprague, Functional localization in the cerebellum. I. Organization in longitudinal cortico-nuclear zones and their contribution to the control of posture, both extrapyramidal and pyramidal. *J. Comp. Neurol.* **103**, 105–129 (1955).
77. W. W. Chambers, J. M. Sprague, Functional localization in the cerebellum. II. Somatotopic organization in cortex and nuclei. *AMA Arch. Neurol. Psychiatry* **74**, 653–680 (1955).
78. K. A. Coffman, R. P. Dum, P. L. Strick, Cerebellar vermis is a target of projections from the motor areas in the cerebral cortex. *Proc. Natl. Acad. Sci. U.S.A.* **108**, 16068–16073 (2011).
79. L. Suzuki, P. Coulon, E. H. Sabel-Goedknegt, T. J. H. Ruigrok, Organization of cerebral projections to identified cerebellar zones in the posterior cerebellum of the rat. *J. Neurosci.* **32**, 10854–10869 (2012).
80. J. U. Henschke, J. M. Pakan, Disynaptic cerebrocerebellar pathways originating from multiple functionally distinct cortical areas. *eLife* **9**, e59148 (2020).
81. W. Heffley *et al*., Coordinated cerebellar climbing fiber activity signals learned sensorimotor predictions. *Nat. Neurosci.* **21**, 1431–1441 (2018).
82. I. Carta, C. H. Chen, A. L. Schott, S. Dorizan, K. Khodakhah, Cerebellar modulation of the reward circuitry and social behavior. *Science* **363**, eaav0581 (2019).
83. D. Kostadinov, M. Beau, M. Blanco-Pozo, M. Häusser, Predictive and reactive reward signals conveyed by climbing fiber inputs to cerebellar Purkinje cells. *Nat. Neurosci.* **22**, 950–962 (2019).
84. N. Larry, M. Yarkoni, A. Lixenberg, M. Joshua, Cerebellar climbing fibers encode expected reward size. *eLife* **8**, e46870 (2019).
85. N. Sendhilnathan, M. Semework, M. E. Goldberg, A. E. Ipata, Neural correlates of reinforcement learning in mid-lateral cerebellum. *Neuron* **106**, 188–198.e5 (2020).
86. National Research Council, *Guide for the Care and Use of Laboratory Animals* (National Academies Press, Washington, DC, ed. 8, 2011).
87. C. J. Guenthner, K. Miyamichi, H. H. Yang, H. C. Heller, L. Luo, Permanent genetic access to transiently active neurons via TRAP: Targeted recombination in active populations. *Neuron* **78**, 773–784 (2013).
88. I. R. Wickersham, H. A. Sullivan, H. S. Seung, Production of glycoprotein-deleted rabies viruses for monosynaptic tracing and high-level gene expression in neurons. *Nat. Protoc.* **5**, 595–606 (2010).
89. G. Paxinos, K. B. J. Franklin, *The Mouse Brain in Stereotaxic Coordinates* (Academic Press, ed. 4, 2013).
90. E. A. Pnevmatikakis, A. Giovannucci, NoRMCorre: An online algorithm for piecewise rigid motion correction of calcium imaging data. *J. Neurosci. Methods* **291**, 83–94 (2017).